Fluidic Oscillator Performance under Several Mixing Chamber Dimensional Modifications

Kavoos Karimzadegan , Masoud Mirzaei , Josep M. Bergadà *

Posted Date: 11 January 2024

doi: 10.20944/preprints202401.0827.v1

Keywords: Fluidic oscillators design; Computational Fluid Dynamics (CFD); flow control; feedback channel performance

Article

Fluidic Oscillator Performance under Several Mixing Chamber Dimensional Modifications

Kavoos Karimzadegan [1], Masoud Mirzaei [2] and Josep M. Bergada [1,*]

[1] Fluid Mechanics Department, Universitat Politècnica de Catalunya, 08034 Barcelona, Spain
[2] Faculty of Aerospace engineering, K.N.Toosi University of Technology, Tehran, Iran
* Correspondence: josep.m.bergada@upc.edu; Tel.: +34-937398771

Abstract: In Active Flow Control (AFC) applications, to activate the boundary layer the use of pulsating flow has notorious energy advantages versus constant blowing/suction jet injections. For a given AFC application, five parameters, jet location and width, inclination angle, frequency of injection and momentum coefficient need to be tuned. Two main devices are nowadays capable of injecting pulsating flow with the sufficient momentum coefficient to delay the boundary layer separation, these are the Zero Net Mass Flow actuators (ZNMFA) and the Fluidic Oscillators (FO). In the present research, a novel FO configuration is analyzed for the first time at relatively high Reynolds numbers, fluid is considered as incompressible. After obtaining the typical linear correlation between the incoming Reynolds number and the outlet flow oscillating frequency, the effect of outlet width and mixing chamber wedge inclination angle dimensional modifications is addressed, modifications of the outlet width are observed to create large variations on the FO performance. The origin of the self-sustained oscillations is also analyzed in the present manuscript and greatly helps in clarifying the forces acting on the jet inside the mixing chamber. In fact we can conclude saying that the current FO configuration is pressure driven although the mass flow forces appear to be a much more relevant than in previous FO configurations studied.

Keywords: fluidic oscillators design; Computational Fluid Dynamics (CFD); flow control; feedback channel performance

1. Introduction

Among the wide range of applications the Fluidic Oscillators (FO) can be employed in, it is relevant to highlight their use to enhance mixing [1,2], as heat transfer enhancers [3,4], as sensors to measure fluid flow [5–7], as fluidic sensors to measure micro/nanoscale transport properties [8], and can serve as well as acoustic biosensors [9,10]. Perhaps the most common application is their use as an Active Flow Control (AFC) device to delay the boundary layer separation on bluff bodies [11–13]. The use of pulsating flow in AFC applications provides the advantage of reducing the energy required to alter the boundary layer around bluff bodies. When considering options for producing pulsating jets, Zero Net Mass Flux Actuators (ZNMFA) and Fluidic Oscillators (FO) stand out as promising choices. Notably, FO has a distinct advantage because it relies on stationary components, enhancing its reliability. While the range of canonical shapes for FO is somewhat restricted, delving into its performance becomes especially meaningful when tweaking internal dimensions. This involves examining variations in oscillation amplitude and frequency. The main objective of this paper is to shed light on this subject. In 2013, Bobusch et al. [14] carried out one of the initial assessments of fluidic oscillator performance by modifying its internal configuration. They provided recommendations concerning the inlet width of the mixing chamber to alter the output frequency of the fluidic actuator. Prior to this, in 2012, Vatsa et al. [15] investigated two different configurations of sweeping jet fluidic oscillators (FO) using the lattice Boltzmann method and the PowerFLOW solver. Following this research, Ostermann et al. [16] conducted a more in-depth examination of these configurations in 2015. The two fluidic oscillators (FO) under examination bear similarities to those studied by Bobusch et al. [14] and Aram et al. [17], respectively. The velocity profiles generated by the FOs in quiescent

 doi:10.20944/preprints202401.0827.v1

air were compared with experimental data. The findings suggested that the FO with sharp internal corners, resembling the one employed in the research by [14], produced a notably more consistent output velocity distribution in comparison to the oscillator with rounded internal corners. An analysis was conducted to compare the results of the two distinct setups, aiming to identify similarities and differences between the designs. Additionally, insights were provided into how these variations could potentially affect applications. Woszidlo et al. [18], examined a configuration that had been previously assessed by Gaertlein et al. [19]. Both of these configurations shared similarities with the one used by Bobusch et al. [14], with the main differences observed in the resulting output shape. In both [18] and [19], attention was centered on a single output. Indeed, Woszidlo et al. [18] directed their focus towards a thorough examination of flow phenomena within the mixing chamber and feedback channels. They observed that increasing the inlet width of the mixing chamber tended to raise the output frequency. Moreover, they discovered that introducing rounded features into the feedback channels led to a decrease in the formation of separation bubbles along these channels. Slupski and Kara [20] employed 2D-URANS simulations using Fluent software to investigate various geometry parameters for feedback channels (FC). The design of the sweeping jet actuator resembled the one examined by Aram et al. [17]. The study explored the impact of changing feedback channel height and width at different mass flow rates. All simulations were carried out under conditions of fully turbulent compressible flow, using the SST k-omega turbulence model. The results indicated that oscillation frequencies increased with increasing the feedback channel height up to a certain threshold, beyond which they remained unchanged. On the flip side, frequencies showed a decrease with the additional expansion of the feedback channel width. Wang et al. [21] carried out both experimental and numerical studies on a fluidic oscillator capable of producing frequencies across a wide range (50-300 Hz). Their investigation centered on examining the oscillation frequency response in relation to different lengths of the feedback channels. To accomplish this, they utilized 2D compressible simulations with the sonicFoam software and applied the k-epsilon turbulence model. Significantly, their results revealed a reverse linear correlation between frequency and the length of feedback loops. More precisely, decreasing the length of the feedback channel resulted in an increase in frequency. In 2018, Pandey and Kim [22] performed a three-dimensional numerical simulation, using the SST turbulent model, on the identical configuration previously employed by [14]. In this iteration, a single exit was employed, and the investigation was carried out at a Reynolds number of 30000. Two geometric parameters, specifically the inlet and outlet widths of the mixing chamber, underwent adjustments. Significantly, modifying the inlet width had a significant influence on both the flow structure and the flow rate within the feedback channel, whereas minimal effects were noted when adjusting the outlet width. Investigating the impacts of changing the lengths of the feedback channel (FC) and the mixing chamber (MC) on output frequency and amplitude, were performed by Seo et al. [23], they utilized a 2D numerical model in 2018. The simulations were conducted assuming incompressible flow, with a Reynolds number of 5000. Intriguingly, it was noted that elongating the feedback channel length did not bring about any alterations in the output frequency. This observation had been previously noted by [24], and both studies adopted incompressible flow assumptions, limiting the precision of the simulations in delivering precise information. In contrast, elongating the length of the mixing chamber resulted in a noticeable decrease in the actuator's output frequency. Baghaei and Bergada [25] developed 3D simulation for a 3D fluidic Oscillator. They implemented a comprehensive analysis on the forces driving the oscillations. In 2020 they used the same model and studied the effect of several design modifications [26]. Bergada et al. [27] studied the effect of feedback channel (FC) length on FOs performance for compressible flows conditions, they found out that at large feedback channel lengths, the former main oscillation tends to disappear, the jet inside the mixing chamber simply fluctuates at high frequencies and as the Feedback Channel (FC) length exceeds a certain threshold the FO stops oscillating. In Sarvar et al. [28], it was studied a novel shape of fluidic scillator (FO) in the laminar regime at very low Reynolds number, they observed the jet sweeping angle amplitude is more pronounced for the two-dimensional FO as compared to three-dimensional at a fixed given

 doi:10.20944/preprints202401.0827.v1

Reynolds number and the instability of the output jet, becomes slightly chaotic at very low Reynolds numbers. In recent years many researchers have been working on analysis, design, and applications of FO's. For instance, Lee et al. [29], performed a numerical study of the influence of jet parameters of fluidic oscillator-type fuel injector on the mixing performance in a supersonic flow field. Their results showed that the influence of the sweeping jet angle on the mixing performance is more notable than that of the oscillating frequency and they concluded that an appropriate combination of the frequency and sweeping jet angle to maximize the mixing performance is needed. In another attempt, Takavoli et al. [30] conducted a numerical investigation for enhancing a subsonic ejector performance by incorporating a fluidic oscillator as the primary nozzle. Their results indicated that a harmonically oscillating primary flow was generated, increasing the mixing entrainment and momentum transfer while reducing the pressure in the suction and mixing chambers.

In this research, a newly designed fluidic oscillator (FO), previously studied by [28] at very low Reynolds numbers is analyzed using numerical methods at relatively high Reynolds numbers, flow is assumed as incompressible. Following the establishment of a typical linear correlation between the Reynolds number and the oscillating frequency of the outlet flow, the study addresses the impact of dimensional modifications in outlet width and mixing chamber wedge inclination angle. Notably, alterations in the outlet width are observed to have a substantial influence on the performance of the fluidic oscillator. The manuscript also delves into the analysis of the origin of self-sustained oscillations, providing valuable insights into the forces acting on the jet within the mixing chamber. Ultimately, it is deduced that the current FO configuration operates under pressure-driven conditions, although mass flow forces appear to be much more significant than in previously studied FO configurations [25,26].

2. Governing Equations and Turbulence Model

In Computational Fluid Dynamics (CFD) simulations and when considering the fluid as incompressible, Navier-Stokes (NS) equations take the form:

$$\frac{\partial u_i}{\partial x_i} = 0 \tag{1}$$

$$\frac{\partial u_i}{\partial t} + \frac{\partial u_i u_j}{\partial x_j} = -\frac{1}{\rho}\frac{\partial p}{\partial x_i} + \nu \frac{\partial^2 u_i}{\partial x_j \partial x_j} \tag{2}$$

If the fluid is considered as turbulent, several approaches to solve NS equations are possible, ideally Direct Numerical Simulation (DNS) should be employed, the main problem associated to DNS is the extremely small mesh cells and time steps required, then the Kolmogorov length and time scales should be reached to properly detect the energy dissipation range. In the vast majority of the applications the mentioned drawbacks makes impossible to use DNS, simply because the computational time is far too large. The second approach is the use of Large Eddy simulation (LES) as turbulence model, it is a very good option in 3D flows, yet it still requires very fine meshes and large computational times. LES requires a Subgrid Scale Model (SGS) which is used in areas where the vortical structures are smaller than the dimension of the mesh cells. Nowadays LES turbulence modelling is extensively used although the computational time required, despite the fact supercomputers are being used, is still too large for many applications. As a result, the vast majority of the nowadays CFD applications still need to be performed using Reynolds Averaged Navier Stokes (RANS) or URANS unsteady-RANS turbulence models. Their precision is not as accurate as LES or DNS ones, but the computational time needed shortens drastically and allows performing 2D-CFD simulations with a reasonable degree of accuracy.

To discretize the NS equations under incompressible flow conditions, it needs to keep in mind that the only variables associated to the NS equations are the pressure and the three velocity components. In order to be able to apply URANS models, each variable from the NS equations (we will call ϕ any generic variable) need to be substituted by its average $\bar{\phi}$ and a fluctuation ϕ'term.

Preprints (www.preprints.org) | NOT PEER-REVIEWED | Posted: 11 January 2024 doi:10.20944/preprints202401.0827.v1

$$\phi = \bar{\phi} + \phi' \tag{3}$$

Once the mentioned substitution is performed, the resulting NS equations take the form: (here just the equations for two dimensional CFD models are presented).

$$\frac{\partial \rho}{\partial t} + \frac{\partial \rho \bar{u}_x}{\partial x} + \frac{\partial \rho \bar{u}_y}{\partial y} = 0 \tag{4}$$

$$\begin{aligned} \rho\left(\frac{\partial \bar{u}_x}{\partial t} + \bar{u}_x\frac{\partial \bar{u}_x}{\partial x} + \bar{u}_y\frac{\partial \bar{u}_x}{\partial y}\right) = &-\frac{\partial p}{\partial x} + \rho g_x + \frac{\partial}{\partial x}\left(2\mu\frac{\partial \bar{u}_x}{\partial x} - \rho(\bar{u}_x')^2\right) \\ &+\frac{\partial}{\partial y}\left(\mu\left(\frac{\partial \bar{u}_x}{\partial y} + \frac{\partial \bar{u}_y}{\partial x}\right) - \rho\overline{u_x' u_y'}\right) \end{aligned} \tag{5}$$

$$\begin{aligned} \rho\left(\frac{\partial \bar{u}_y}{\partial t} + \bar{u}_x\frac{\partial \bar{u}_y}{\partial x} + \bar{u}_y\frac{\partial \bar{u}_y}{\partial y}\right) = &-\frac{\partial p}{\partial y} + \rho g_y + \frac{\partial}{\partial x}\left(\mu\left(\frac{\partial \bar{u}_y}{\partial x} + \frac{\partial \bar{u}_x}{\partial y}\right) - \rho\overline{u_y' u_x'}\right) \\ &+\frac{\partial}{\partial y}\left(2\mu\frac{\partial \bar{u}_y}{\partial y} - \rho(\bar{u}_y')^2\right) \end{aligned} \tag{6}$$

All RANS turbulence models are based on solving the Navier-Stokes equations by incorporating the concept of turbulence viscosity (μ_t). which can be mathematically added into the momentum equations described above using the subsequent differential definition (via the Boussinesq hypothesis):

$$\mu_t = \frac{-\rho\overline{u_x' u_x'}}{2\frac{\partial \bar{u}_x}{\partial x}} = \frac{-\rho\overline{u_y' u_y'}}{2\frac{\partial \bar{u}_y}{\partial y}} = \frac{-\rho\overline{u_x' u_y'}}{\frac{\partial \bar{u}_x}{\partial y} + \frac{\partial \bar{u}_y}{\partial x}} \tag{7}$$

In fact, the time averaged fluctuation terms are usually grouped in a tensor called the apparent Reynolds stress tensor (τ_{app}), which is a 3×3 symmetric matrix. Note that in the case of two-dimensional flow, this matrix explicitly consists of four terms.

The X and Y momentum terms of the NS equations can therefore be given as:

$$\rho\frac{\partial \bar{u}_x}{\partial t} + \rho\bar{u}_x\frac{\partial \bar{u}_x}{\partial x} + \rho\bar{u}_y\frac{\partial \bar{u}_x}{\partial y} = \rho g_x - \frac{\partial p}{\partial x} + \frac{\partial}{\partial x}\left(2(\mu + \mu_t)\frac{\partial \bar{u}_x}{\partial x}\right) + \frac{\partial}{\partial y}\left((\mu + \mu_t)\left(\frac{\partial \bar{u}_x}{\partial y} + \frac{\partial \bar{u}_y}{\partial x}\right)\right) \tag{8}$$

$$\rho\frac{\partial \bar{u}_y}{\partial t} + \rho\bar{u}_x\frac{\partial \bar{u}_y}{\partial x} + \rho\bar{u}_y\frac{\partial \bar{u}_y}{\partial y} = \rho g_y - \frac{\partial p}{\partial y} + \frac{\partial}{\partial x}\left((\mu + \mu_t)\left(\frac{\partial \bar{u}_x}{\partial y} + \frac{\partial \bar{u}_y}{\partial x}\right)\right) + \frac{\partial}{\partial y}\left(2(\mu + \mu_t)\frac{\partial \bar{u}_y}{\partial y}\right) \tag{9}$$

For the present study we have decided to use the $k-\omega$ SST turbulence model which rely on using the $k-\omega$ model near the wall, the $k-\epsilon$ model far away from the object and a blending function between these two. For the chosen model, the turbulence viscosity μ_t can mathematically be given as:

$$\mu_t = \frac{\rho k}{\omega} \quad \longrightarrow \quad \begin{cases} \rho : \text{density} \\ k : \text{turbulent kinetic energy} \\ \omega : \text{turbulent kinetic energy specific dissipation rate} \end{cases}$$

This model employs two transport equations in order to solve k and ω. The equations used for each parameter are:

$$\frac{\partial k}{\partial t} + u_j\frac{\partial k}{\partial x_j} = P_k - \beta^* k\omega + \frac{\partial}{\partial x_j}\left[(\nu + \sigma_k\nu_T)\frac{\partial k}{\partial x_j}\right] \tag{10}$$

Preprints (www.preprints.org) | NOT PEER-REVIEWED | Posted: 11 January 2024 doi:10.20944/preprints202401.0827.v1

$$\frac{\partial \omega}{\partial t} + u_j \frac{\partial \omega}{\partial x_j} = \alpha S - \beta \omega^2 + \frac{\partial}{\partial x_j}\left[(\nu + \sigma_\omega \nu_T)\frac{\partial \omega}{\partial x_j}\right] + 2(1 - F_1)\sigma_{\omega 2}\frac{1}{\omega}\frac{\partial k}{\partial x_i}\frac{\partial \omega}{\partial x_i} \tag{11}$$

F_1 and F_2 are the blending functions which value depends on the distance of the cell to the wall. The first blending function takes the value of 0 far away from the wall, 1 in the cells close to the wall and values between 0 and 1 in the transition region. The second blending function F_2 depends on the perpendicular distance from the wall (d) and according to [31], since the modification to the eddy-viscosity has its largest impact in the wake region of the boundary layer, it is imperative that F_2 extends further out into the boundary-layer than F_1. Mathematically is expressed as:

$$F_2 = \tanh\left(\arg_2^2\right) \tag{12}$$

$$\arg_2^2 = \max\left(\frac{2k}{\beta^* \omega d}; \frac{500\nu}{\omega d^2}\right) \tag{13}$$

The constants of the arg function are adjusted manually, and for the present case the values of the used turbulence model taken are: $\alpha_1 = 0.556$, $\alpha_2 = 0.44$, $\beta^* = 0.09$, $\beta_1 = 0.075$, $\beta_2 = 0.0828$ $\sigma_{k1} = 0.85$, $\sigma_{k2} = 1$, $\sigma_{\omega 1} = 0.5$, $\sigma_{\omega 2} = 0.856$. Additionally, for a more detailed information of the $k - \omega$ SST turbulence model proposed, see [31].

3. Mesh Assessment

Figure 1 introduces the central part of the (FO) investigated in the present study. The mixing chamber (MC) is the core of the FO, above and below it the Feedback channels (FC) can be observed. Flow enters through the power nozzle (PN) and leaves through the main outlet. The red line shown in the mixing chamber upper converging wall, is simply a line probe to be able to measure the maximum stagnation pressure in this location, although not shown in the figure, the same line probe was placed as well at the lower converging wall. This configuration is called the baseline case and in the present manuscript the main effect on the FO performance when modifying the outlet width and the inlet angle is analysed. Figure 1 also shows the positive and negative directions taken for each of the two geometry modifications.

A fully structured two dimensional (2D) mesh with 367720 cells was used to evaluate the flow at a Reynolds number Re=54595, the characteristic length being the fluidic oscillator power nozzle. in fact, and in order to obtain simulated results independent of the mesh resolution, initially four different mesh densities were evaluated, their respective number of cells were, 62143; 180065; 367720 and 718920. Table 1 summarizes the minimum, maximum and average $y+$ as well as the outlet mass flow frequency associated, obtained for the different mesh resolutions. The last column indicates the frequency error versus the frequency obtained using the denser mesh, notice that the error gathered using a mesh of 367720 cells is negligible. Figure 2a presents the entire computational domain with the mesh associated, a zoomed view of the mesh employed in the FO is shown in Figure 2b, and Figure 2c introduces a zoomed view of the upper feedback channel mesh.

Table 1. Results from the mesh independence study.

Mesh assessment					
2D mesh cells	Min y+	Average y+	Max y+	Frequency (Hz)	Error %
62143 cells	0.007893928	5.255150	63.09918	24.525 Hz	15.37%
180065 cells	0.5630300	1.616285	16.79723	29.181 Hz	0.69%
367720 cells	0.2748158	0.9271403	8.044681	29.091 Hz	0.38%
718920 cells	0.2741867	0.7549317	8.368831	28.98 Hz	-

Preprints (www.preprints.org) | NOT PEER-REVIEWED | Posted: 11 January 2024 doi:10.20944/preprints202401.0827.v1

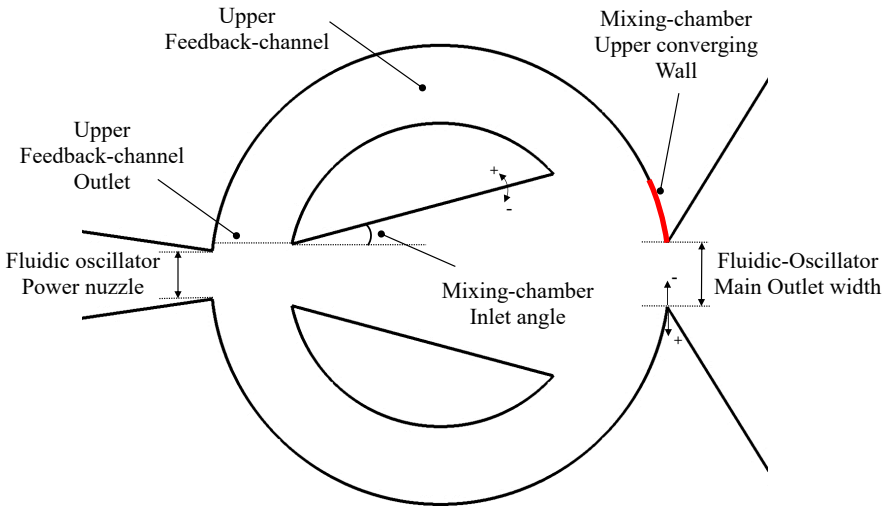

Figure 1. Fluidic oscillator mixing chamber internal dimensions modifications.

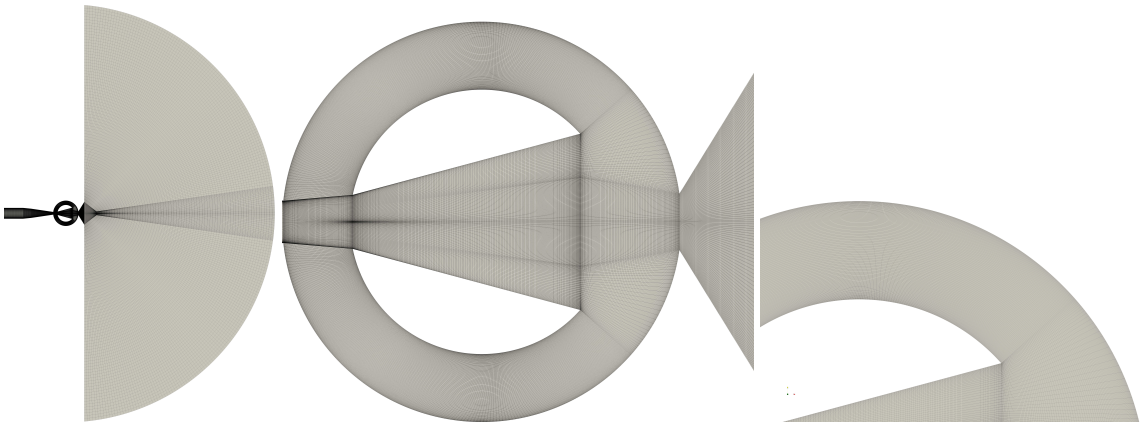

(**a**) (**b**) (**c**)

Figure 2. Grid used in the present study. (a) Computational domain general view, (b) Fluidic Oscillator zoomed view, (c) Upper feedback channel zoomed view.

The boundary conditions employed in all simulations were, Dirichlet for velocity and Neumann for pressure at the inlet. An absolute pressure of 10^5 Pa and Neumann boundary conditions for velocity were considered at the buffer zone outlet. Neumann boundary conditions for pressure and Dirichlet for velocity were set to all walls. Considering a turbulent intensity of 0.1%, the values for the turbulent kinetic energy k, specific dissipation range ω and the turbulent kinematic vicosity ν_t at the inlet were respectively, $k = 2.45 \times 10^{-3}(m^2/s^2)$, $\omega = 2.47(s^{-1})$ and $\nu_t = 9.9 \times 10^{-4}(m^2/s)$. Table 2 summarizes the boundary conditions employed.

In the present study the flow was considered as turbulent, incompressible and isothermal, all simulations were two dimensional. The fluid used was air at 15 degrees Celsius, being the dynamic viscosity and the density $\mu = 1.802 * 10^{-5} Kg/(ms)$ and $\rho = 1.225 Kg/m^3$, respectively. The software OpenFOAM was employed for all simulations, finite volumes is the approach OpenFOAM uses to discretise Navier Stokes equations. Inlet turbulence intensity was set to 0.1% in all cases, Pressure Implicit with Splitting Operators (PISO), was used to solve the Navier Stokes equations, the time step being of 4×10^{-7}s, spatial discretization was set to second order.

Preprints (www.preprints.org) | NOT PEER-REVIEWED | Posted: 11 January 2024 doi:10.20944/preprints202401.0827.v1

Table 2. Summary of the boundary conditions for the baseline case. Reynolds number = 54595

	Boundary conditions				
	k (m^2/s^2)	**omega** (s^{-1})	**nut** (m^2/s)	**P** (Pa)	**U** (m/s)
inlet	$2.45 \cdot 10^{-3}$	2.47	$9.9 \cdot 10^{-4}$	zeroGradient	$u_x = 10$
outlet	zeroGradient	zeroGradient	zeroGradient	10^5	zeroGradient
Top & Bottom	empty	empty	empty	empty	empty
walls	10^{-20}	omegaWallFunction value = 10^5	nutLowReWallFunction value = 0	zeroGradient	0

In order to further check the accuracy obtained with the different mesh densities, we decided to analyze some dynamic characteristics and introduce them in Figure 3. The FO outlet mass flow pulsating frequency is presented in Figure 3a. The instantaneous outlet mass flow and the lower feedback channel mass flow are shown in Figures 3b and 3c, respectively. The dynamic stagnation pressure measured at the Mixing chamber lower converging wall is introduced in Figure 3d. Regardless of the graph chosen it is observed that the dynamic results obtained with the meshes of 367720 and 718920 cells, are almost identical, clear differences are seen when using lower resolution meshes. At this point we can conclude that the mesh of 367720 cells is perfectly good to perform the required simulations.

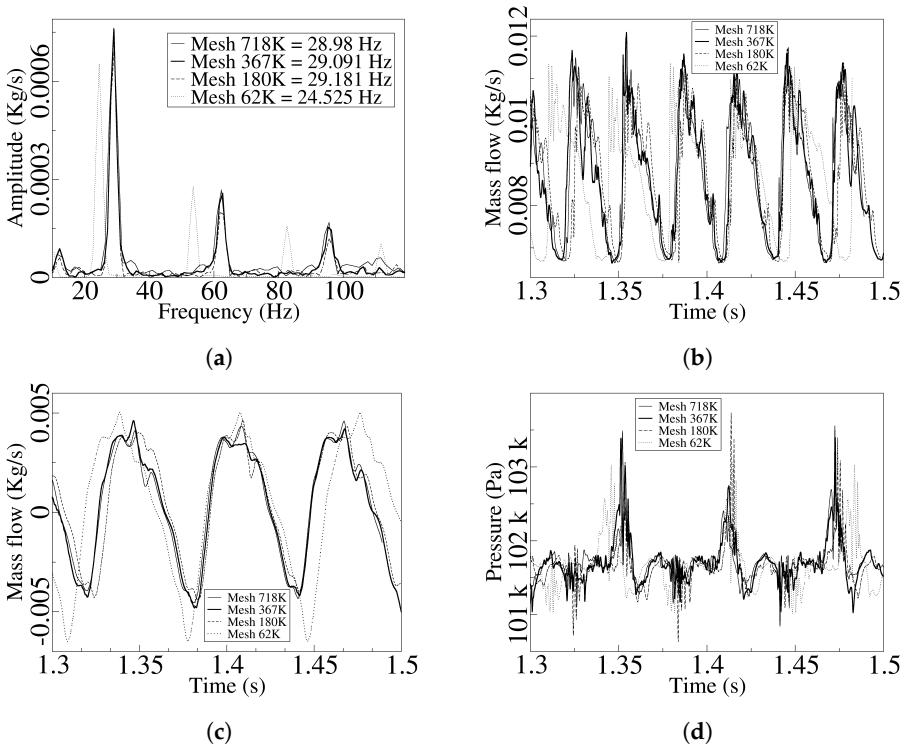

Figure 3. Fluidic oscillator performance at Reynolds number Re= 54595 and for the four different mesh densities considered. Outlet mass flow frequency (a). Outlet mass flow (b). Lower feedback channel mass flow (c). Stagnation pressure measured at the Mixing Chamber downwards converging wall (d).

4. Geometrical Modifications Considered

In the present research, a parametric analysis was performed to analyze the FO main characteristics under different geometrical modifications while keeping the Reynolds number constant at $Re = 54595$. Two different modifications were considered, the mixing chamber outlet with and the mixing chamber inlet angle. Seven different outlet widths ranging between 50% and 150% of the baseline outlet width, and three inlet angles comprised between 79.61% and 122.55% of the baseline inlet angle were

Preprints (www.preprints.org) | NOT PEER-REVIEWED | Posted: 11 January 2024 doi:10.20944/preprints202401.0827.v1

evaluated. Their different dimensions and percentages associated are presented in Table 3 and Table 4, respectively.

Table 3. The different mixing chamber outlet widths considered in the present study.

Outlet widths evaluated							
Outlet width in %	$D_1 = 50\%D_4$	$D_2 = 75\%D_4$	$D_3 = 87.5\%D_4$	$D_4 = (Baseline)$	$D_5 = 112.5\%D_4$	$D_6 = 125\%D_4$	$D_7 = 150\%D_4$
Outlet width in (m)	$0.01333\hat{3}$	0.02	$0.02333\hat{3}$	$0.02666\hat{6}$	0.03	$0.03333\hat{3}$	$0.03999\hat{9}$
Outlet section name	1	2	3	*STD*	4	5	6

Table 4. The different mixing chamber angles considered in the present study.

Mixing chamber inlet angles			
Inlet angle in %	$\alpha_1 = 79.61\%\alpha_2$	$\alpha_2 = (Baseline)$	$\alpha_3 = 122.55\%\alpha_2$
Inlet angle in (degrees)	11.9402	14.9968	18.3788

5. Concept of Momentum, Pressure and Mass Flow Terms, Acting on the Jet Entering the Mixing Chamber

To be able to evaluate the lateral forces pushing the jet as it enters the mixing chamber, the momentum terms on the (FC) outlets is determined. Momentum is characterized by two terms, the pressure and the mass flow one. Both terms were instantaneously evaluated at the feedack channels upper and lower outlets, see Figure 1, the equation considered takes the form:

$$M = \dot{m}_{out} * V_{out} + P_f * S_{out} = \dot{m}_{out}^2/(S_{out} * \rho) + P_f * S_{out} \tag{14}$$

where, $\dot{m}_{out}, V_{out}, S_{out}$ and P_f, are respectively the FC outlet instantaneous mass flow defined as $\dot{m} = \int_s \rho \vec{V} d\vec{s}$, the spatial averaged fluid velocity, the (FC) outlet surface and the spatial averaged pressure instantaneously appearing at any of the FC outlets, ρ is the fluid density. The momentum considered was the one acting on the vertical direction. The net momentum acting on the jet entering the (MC), is obtained when considering the vertical forces defined by Equation (14) acting instantaneously on both (FC) outlets. In this study the fluid is considered as incompressible, fluid density is time and spacial independent but fluid velocity and pressure are spatial and temporal dependent. Therefore to maximize the precision of the calculations, the instantaneous momentum equation to be applied at each FC outlet was discretized and evaluated at each grid cell belonging to the corresponding surface. The resulting equation reads.

$$M = M_{massflow} + M_{pressure} = \rho \sum_{i=1}^{i=n} (S_i V_i^2) + \sum_{i=1}^{i=n} P_i S_i \tag{15}$$

The subindex i denotes any mesh cell belonging to the FC outlet surface. The term n defines the total number of cells corresponding to any of the two FC outlet surfaces. P_i and V_i characterize the instantaneous pressure and velocity components acting on the corresponding mesh cell in vertical direction. In the present paper, the instantaneous momentum term due to the mass flow was obtained simply by adding the elementary momentum terms of each mesh cell belonging to the chosen surface. The momentum pressure term was obtained when multiplying the instantaneous static pressure acting on each cell by the cell surface, and then adding the elemental momentum pressure terms

Preprints (www.preprints.org) | NOT PEER-REVIEWED | Posted: 11 January 2024 doi:10.20944/preprints202401.0827.v1

corresponding to the surface under study. Just the momentum in the vertical direction was considered in all cases.

6. Results

6.1. Reynolds Number Modification

One of the main characteristics of any fluidic oscillator is its linear relation between the inlet Reynolds number and the output mass flow frequency. Four Reynolds numbers, Re=27483, 41224, 54595 and 68707, based on the mixing chamber inlet width and velocity, were simulated to evaluate the actual FO linear performance. The result was a perfect linear behaviour defined by the equation: $f(Hz) = 0.0005364786 * Re - 0.18617977$, being the correlation coefficient: $R^2 = 0.999966$. It needs to be considered that this equation is valid in the range of Reynolds numbers here presented.

The dynamic mass flow at the FO outlet and at the lower FC channel outlet are introduced in Figure 4 for the different Reynolds numbers studied. As Reynolds number increases, the FO outlet mass flow average value and peak to peak amplitude keeps increasing, Figure 4a, amplitude increases by 270% when the Reynolds number raises from 27483 to 68707. The peak to peak amplitude of the FC mass flow suffers a much smaller growth with the Reynolds number increase, just a 159% when comparing the minimum and maximum Reynolds numbers studied, being the average value around zero. In fact, the mass flow across the FC is non symmetric, the mass flow flowing towards the FC outlet at Reynolds number 68707 is about 36% larger than the one flowing towards the FC inlet, the percentage raises to almost 68% for the minimum Reynolds number studied, see Figure 4b. Perhaps one of the most relevant parameter to consider is the stagnation pressure dynamics at the Mixing Chamber (MC) outlet inclined walls. The stagnation pressure oscillations appear to be directly correlated to the momentum pressure and mass flow terms measured at the FC outlet. These three parameters are respectively presented in Figure 5a, c, e. On the right hand side of Figure 5, it is presented the time averaged values of the MC lower inclined wall stagnation pressure, the net momentum time averaged pressure term measured at the lower FC outlet and the time averaged mass flow momentum measured at the same location, see Figure 5b, d, f, respectively. These figures also show the peak to peak amplitude of these variables as a function of the Reynolds number evaluated. The net momentum dynamics obtained when consideing the pressure and mass flow terms measured simultaneously at both feedback channels outlets and for all Reynolds numbers evaluated is presented in Figure 5g, the corresponding time averaged and peak to peak amplitude values are introduced in Figure 5h.

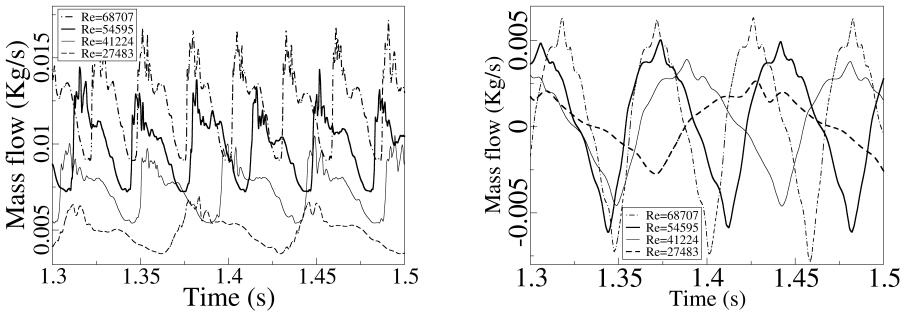

Figure 4. Fluidic oscillator outlet dynamic mass flow (a) and feedback channel mass flow (b), as a function of the Reynolds number.

Preprints (www.preprints.org) | NOT PEER-REVIEWED | Posted: 11 January 2024 doi:10.20944/preprints202401.0827.v1

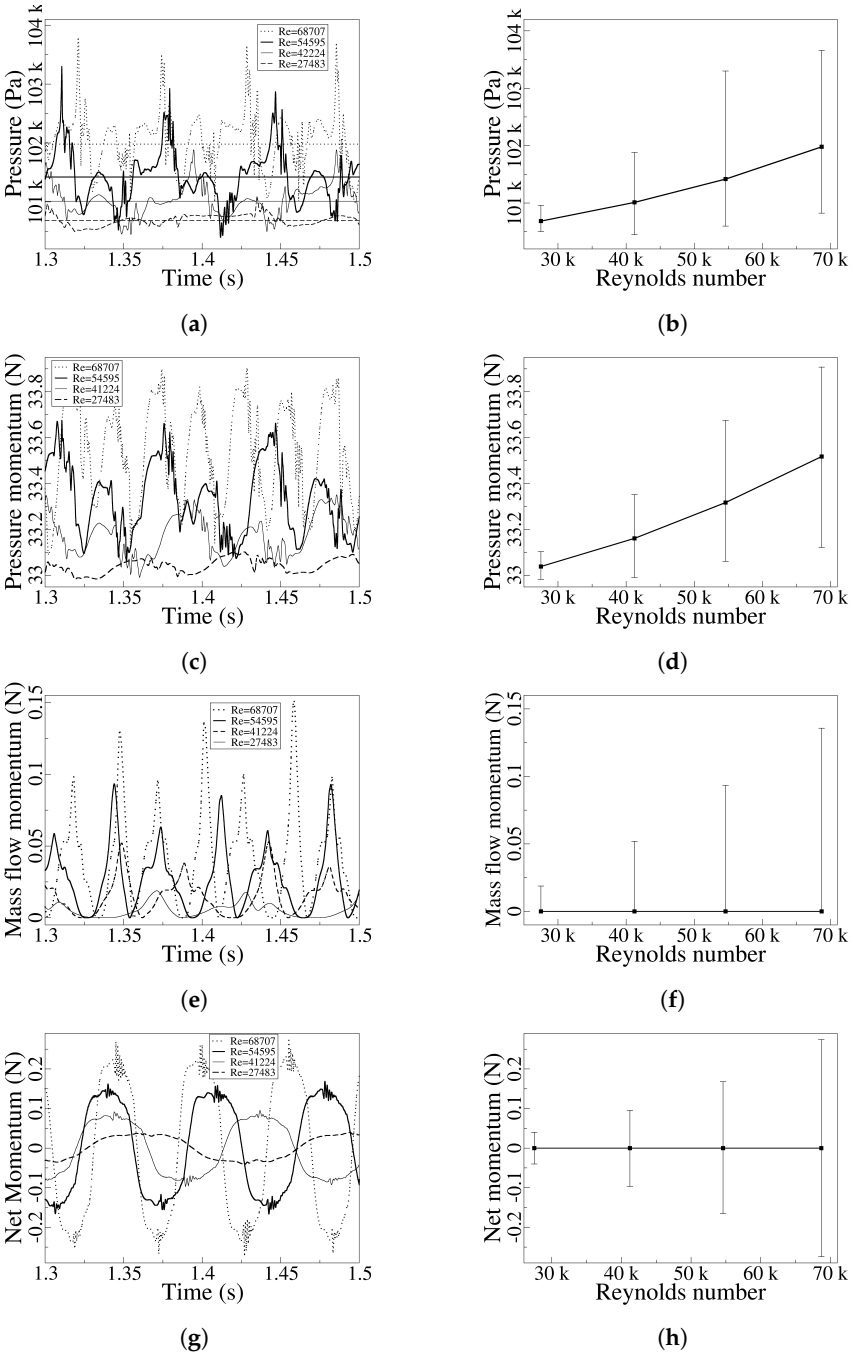

Figure 5. Stagnation pressure dynamics measured at the mixing chamber lower inclined wall (a), time average values and peak to peak amplitudes (b). Pressure momentum term measured at the FC lower outlet (c), and their respective average values and peak to peak amplitudes (d). Dynamic mass flow momentum term measured at the FC lower outlet (e), and their respective average values and peak to peak amplitudes (f). Instantaneous net momentum obtained when considering pressure and mass flow momentum terms at both FC outlets (g), average values and the peak to peak amplitudes (h). All graphs consider the four Reynolds numbers studied.

From the dynamic graphs it appears as if the frequencies associated to the stagnation pressure term measured at the MC inclined wall and for the different Reynolds numbers, are as well observed in the dynamic values representing the pressure momentum, mass flow momentum and net momentum values shown in Figure 5c, e, g, respectively, showing a correlation between all these parameters. In fact the frequencies associated to the different parameters and for the different Reynolds numbers are

Preprints (www.preprints.org) | NOT PEER-REVIEWED | Posted: 11 January 2024 doi:10.20944/preprints202401.0827.v1

presented in Table 5, from where it is demonstrated that a correlation between all these parameters has to exist. Notice that the main frequency is almost identical for all the parameters evaluated.

Table 5. Main frequency as a function of the Reynolds number and the dynamic parameter evaluated.

Reynolds number	**Re=27483**	**Re=41224**	**Re=54595**	**Re-68707**
Parameter	**Main Frequency [Hz]**			
MC wall pressure	7.5	11	14.53	18.55
FC Pressure momentum	7.52	10.86	14.62	18.57
FC Mass flow momentum	7.52	10.88	14.53	18.26
Net momentum	7.25	10.85	14.6	18.25

To further evaluate the link between the four parameters presented in Figure 5, the reader should now focus on Figure 5b, d, f. When comparing the peak to peak amplitude for the three parameters introduced in these figures and considering the minimum and maximum Reynolds numbers analyzed, it is observed that the maximum peak to peak amplitude is about 6.5 times larger than the minimum one, which corresponds to the minimum Reynolds number. In other words, the mixing chamber inclined wall stagnation pressure dynamics is driving the momentum pressure term dynamics as well as the mass flow momentum term dynamics measured at the FC lower outlet. At this point and based on the information presented in Table 5 and Figure 5, we can conclude that the self sustained oscillations appear to be controlled by the stagnation pressure dynamics at the MC inclined walls. To further back up this hypothesis it is relevant to highlight that the momentum pressure term measured at a FC outlet width is nearly three orders of magnitude higher than the mass flow one, Figure 5c and e, respectively. The net momentum is very small compared with the pressure momentum term measured on a FC single outlet, but it is about four times larger than the mass flow momentum of a single FC outlet, compare Figure 5g and e. This clarifies that small variations of the pressure momentum have a deep effect on the net one. To understand the relevance of the pressure net momentum terms versus the mass flow ones, measured instantaneously at both FC outlets, Figure 6 and Figure 7 are generated.

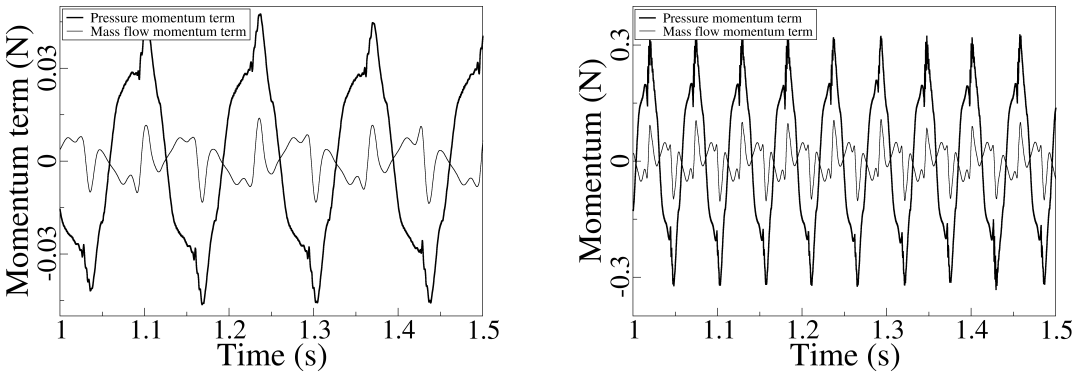

(**a**) (**b**)

Figure 6. Instantaneous net momentum pressure and mass flow terms measured at the feedback channels outlet sections and for the minimum and maximum Reynolds numbers studied. (a) Reynolds number 27483. (b) Reynolds number 68707.

Preprints (www.preprints.org) | NOT PEER-REVIEWED | Posted: 11 January 2024 doi:10.20944/preprints202401.0827.v1

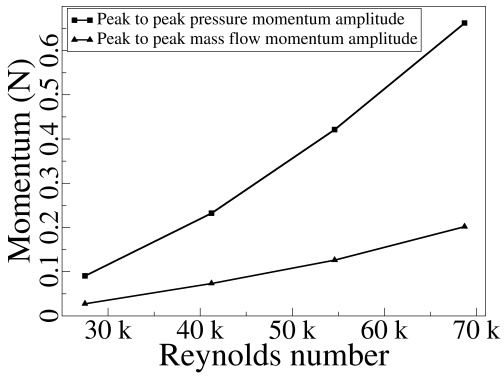

(**a**)

Figure 7. Pressure and mass flow peak to peak net momentum amplitude measured at the feedback channels and for the four Reynolds numbers evaluated.

The first one compares the two dynamic net momentum terms for the minimum and maxim Reynolds numbers studied, where it states that the value of the net momentum pressure term at Re=27483 is 3.27 times larger than the net momentum mass flow term. In fact, the relation between the pressure and mass flow net momentum terms, remains rather constant for all Reynolds numbers studied, this is clearly observed in Figure 7, where the peak to peak amplitude of both net momentum terms is presented for the four Reynolds number evaluated. All these graphs clarify that for the FO configuration presented in this study, the forces acting onto the jet as it enters the mixing chamber are mostly due to the pressure operating at the FC outlets, yet the forces due to the FC mass flow term are the same order of magnitude than the pressure ones. At this point it is important to recall the work done by [25–27], where it was stated that the jet was pressure driven and the mass flow forces were playing a secondary role. The much more relevant role played by the FC mass flow forces in the present FO configuration, it is believed to be due to the particularly short and wide feedback channels employed in the present fluidic oscillator.

Instantaneous FO velocity and pressure fields for the minimum and maximum Reynolds numbers evaluated, Re=27483, and Re=68707, are presented in Figure 8. The instant chosen is the one at which the stagnation pressure value at the MC lower inclined wall is maximum, notice the red spot both pressure fields show at this location. It is as well relevant to observe that both lower FC's are pressurized when compared with the respective upper ones. In fact this figure clarifies that as the Reynolds number increases, the maximum and minimum pressure inside the Mixing Chamber, increases and decreases respectively, see the color bars associated. Four videos showing the FO dynamic velocity and pressure fields for these two Reynolds numbers are introduced in appendix as supplementary material. The videos clarify the rather large reversed flow (from the FC outlet towards the FC inlet) previously introduced in figure Figure 4b, they show as well the pressure and mass flow temporal evolution in the FC's and the mixing chamber

Preprints (www.preprints.org) | NOT PEER-REVIEWED | Posted: 11 January 2024 doi:10.20944/preprints202401.0827.v1

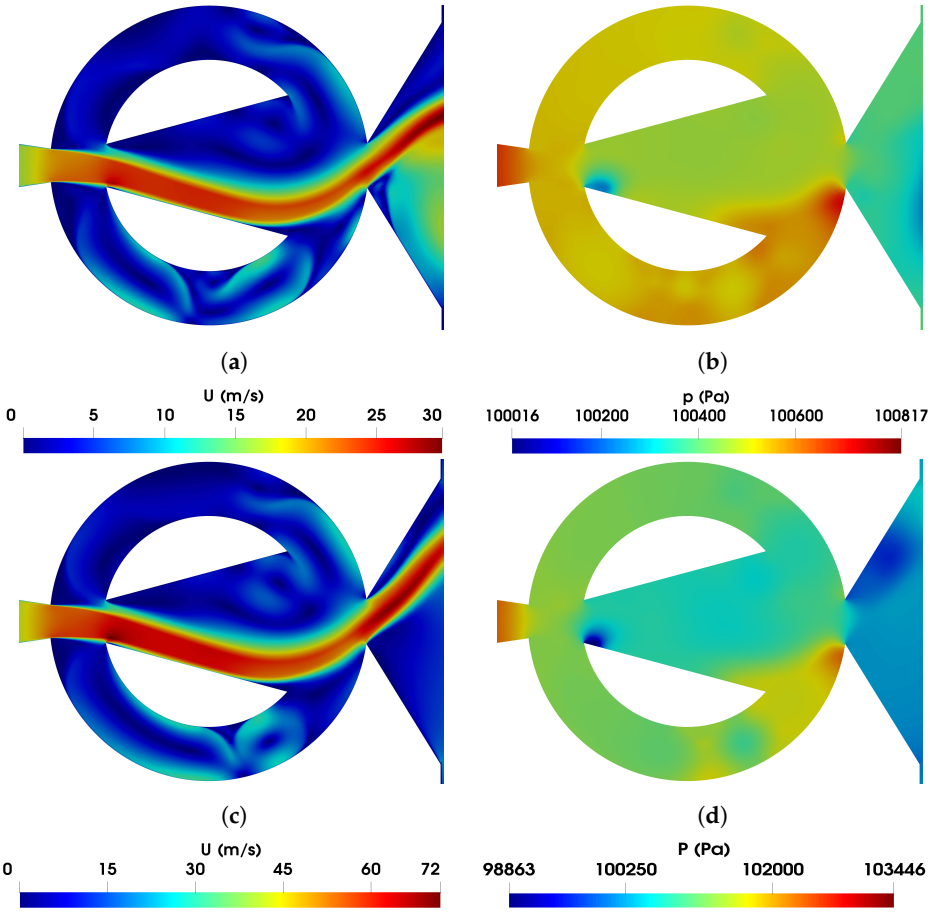

Figure 8. Fluidic oscillator internal velocity magnitude field (a, c) and pressure field (b, d). Minimum Reynolds number $Re = 27483$ (a, b), Maximum Reynolds number $Re = 68707$ (c, d).

6.2. Outlet width Modification

In the present subsection, the same flow parameters previously evaluated as a function of the Reynolds number will now be analyzed for several outlet widths (seven in total) initially defined in Table 3. Notice that in the present section the Reynolds number is kept constant at Re=54595. As previously done for different Reynolds numbers, Figure 9 introduces the FO and FC dynamic mass flows for the smallest (outlet 1), largest (outlet 6) and standard (STD) outlet widths evaluated in the present research. As expected, the FO outlet mass flow average value remains constant, then the incoming flow have a constant Reynolds number. But the peak to peak amplitude drastically grows with the outlet width, in fact the FO outlet mass flow amplitude grows by 286% when comparing the largest (outlet 6) and smallest (outlet 1) widths evaluated, Figure 9a. The FO oscillation frequency reduces by 10% width the outlet width increase, it went from 14.8Hz in (outlet 1) to 13.33Hz in (outlet 6). On the other hand, the FC mass flow, see Figure 9b, appears to be rather unaffected by the outlet width modifications tested, the FC mass flow average value, peak to peak amplitude and frequency, suffer negligible changes, less than 0.5%, when comparing the maximum and minimum outlet widths studied.

What it is perhaps very relevant to highlight is that the FC mass flow is not always flowing from the FC inlet towards the FC outlet, but there is an even larger instantaneous reverse flow, (flow going from the FC outlet towards the FC inlet). This large reverse flow is more clearly seen in the velocity field videos presented in appendix as supplementary material, and it seems to be a particular characteristic of the present FO configuration. Notice that the wide and short FC paths enhance the travelling of the fluid particles in both FC directions. On the other hand the MC inlet width, chosen for the present FO configuration appears to be rather small and so it favors the existence of reverse

Preprints (www.preprints.org) | NOT PEER-REVIEWED | Posted: 11 January 2024 doi:10.20944/preprints202401.0827.v1

flow. It is as well relevant to highlight the existence of flow asymmetry on both the FO outlet and FC mass flows. When the FO outlet mass flows reaches its maximum, the peak is rather scattered, as if the fluid was trembling, but when the outlet mass flow reaches its minimum, which happens when the FO outlet mass flow flows horizontally, the reverse flow in one of the FC and the direct flow in the other FC, both are maximum. Under these conditions the FO outlet mass flow presents rather a smooth minimum peak. Authors believe that the pressure dynamics at the MC outlet inclined walls may explain such behaviour. These details will be carefully addressed in the final section of the paper.

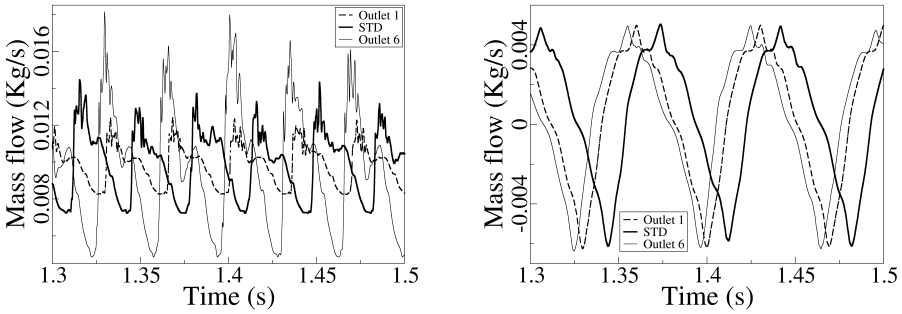

Figure 9. Fluidic oscillator outlet dynamic mass flow (a) and feedback channel mass flow (b), for the smallest (Outlet 1), largest (Outlet 6) and standard (STD) outlet widths evaluated.

The dynamic stagnation pressure measured at the MC outlet lower inclined wall is presented in Figure 10a, from where it can clearly be seen that as the outlet width is reduced the time averaged value as well as the peak to peak amplitude at the MC outlet inclined wall raises. In fact the time averaged pressure at the entire MC and FC's also increases. The time averaged evolution of the dynamic pressure at the MC outlet inclined wall, as well as its peak to peak amplitude for all outlet widths studied is presented in Figure 10b. When comparing the minimum and maximum outlet widths it is observed a time averaged and peak to peak pressure increase of almost 2.3% and 76% respectively. A very similar trend is observed when analyzing the dynamic and time averaged pressure momentum term at the lower FC outlet, see Figure 10c, d. Notice that the time averaged and peak to peak values increase, (when comparing the minimum and maximum outlet widths) is of almost 2% and 74%, respectively, again suggesting a direct correlation between the stagnation pressure at the MC inclined walls and the one at the FC outlet. The mass flow momentum term measured at the lower FC outlet is introduced in Figure 10e. As already observed when evaluating the different Reynolds numbers, the mass flow momentum term is over two orders of magnitude smaller than the pressure momentum one, compare figures Figure 10e and c, therefore indicating the high jet sensitiveness to the pressure forces. But when considering the instantaneous mass flow and pressure momentum terms at both feedback channels outlets, it is observed that the net momentum acting on the jet as it enters the mixing chamber is rather small, Figure 10f, its peak to peak being about three times larger than the mass flow momentum one measured at the lower FC outlet. Notice as well that the net momentum is rather constant for the different outlet widths studied, since the pressure drop between both FC outlets slightly change with the outlet width modifications considered in the present study. In order to see which is the main contributor of the jet self sustained oscillations, the instantaneous pressure momentum term evaluated on both FC outlets is presented for the minimum (outlet 1) and maximum (outlet 6) outlet widths in Figure 11a, b, respectively. For comparison, the dynamic mass flow momentum measured at the same locations and for the same outlets is also presented in the same two figures. For the smallest outlet width considered, (outlet 1) the peak to peak pressure momentum term is about 270% larger than the mass flow one. In fact, the pressure momentum term slightly grows with the outlet width while the mass flow term remains rather constant, their relation being of about 345% for the maximum outlet width, (outlet 6). The main conclusion from Figure 11 is that, the net forces acting on the jet as it enters

Preprints (www.preprints.org) | NOT PEER-REVIEWED | Posted: 11 January 2024 doi:10.20944/preprints202401.0827.v1

the mixing chamber are due to the pressure but the mass flow forces are having the same order of magnitude.

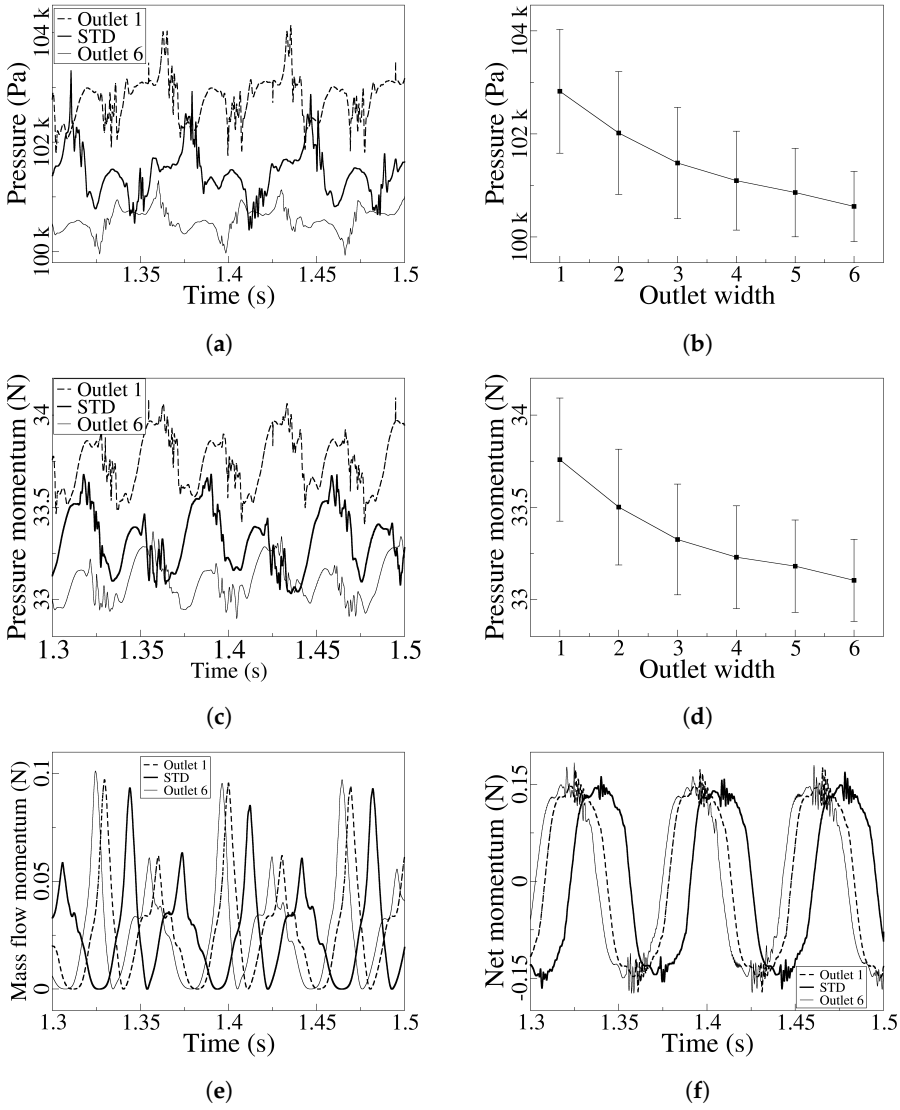

Figure 10. Stagnation pressure dynamics measured at the mixing chamber lower inclined wall (a), time average values and peak to peak amplitudes (b). Pressure momentum term measured at the FC lower outlet (c), and their respective average values and peak to peak amplitudes (d). Dynamic mass flow momentum term measured at the FC lower outlet (e), and the instantaneous net momentum obtained when considering pressure and mass flow momentum terms at both FC outlets (f). All graphs consider three different outlet widths, the smallest, (Outlet 1), the standard case (STD) and the largest one (Outlet 6) studied in the present research.

Instantaneous velocity and pressure fields for the minimum outlet width (outlet 1), standard one and maximum outlet width (outlet 6) are presented in Figure 12. The maximum velocity as well as the maximum pressure is observed to decrease with the outlet width increase. Particularly for the minimum outlet width (outlet 1), the entire FO is pressurized, but regardless of the outlet width it can clearly be seen the high stagnation pressure area on the mixing chamber lower inclined wall, which in fact is what triggers the self sustained oscillations.

Preprints (www.preprints.org) | NOT PEER-REVIEWED | Posted: 11 January 2024 doi:10.20944/preprints202401.0827.v1

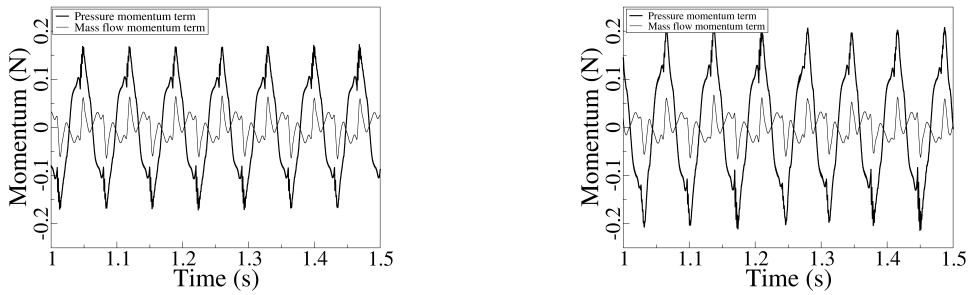

Figure 11. Instantaneous momentum pressure and mass flow terms measured at both feedback channels outlet sections and for the minimum and maximum outlet widths studied. (a) Minimum outlet width (outlet 1). (b) Maximum outlet width (outlet 6).

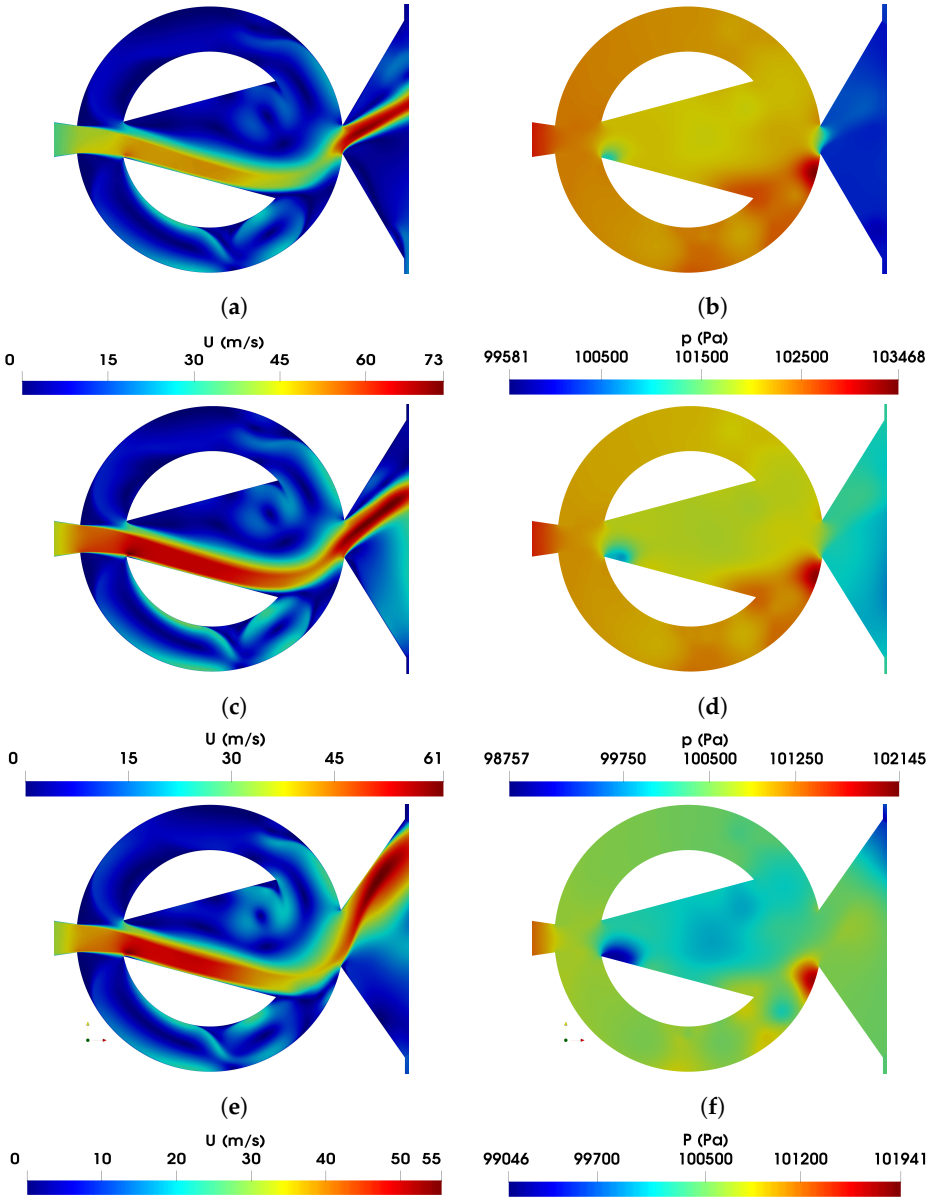

Figure 12. Fluidic oscillator velocity magnitude (a, c, e) and pressure fields (b, d, f), for the minimum (outlet 1) (a, b), standard (c, d) and maximum (outlet6) (e, f) outlet widths evaluated. Reynolds number is kept constant at Re=54595.

Preprints (www.preprints.org) | NOT PEER-REVIEWED | Posted: 11 January 2024 doi:10.20944/preprints202401.0827.v1

To more properly see the dynamics of the velocity and pressure fields, six videos which correspond to the three cases presented in Figure 12 are introduced in appendix as supplementary material. From the videos it is clearly observed the reverse feedback channel mass flow appearing in all the cases studied. As this FO is a novel design never studied at these Reynolds numbers, it clearly requires future work which could address the required dimensional modifications to reduce or even suppress the reverse flow in the feedback channels. In fact the design presented here was mostly created to be able to evaluate the origin of the forces generating the self sustained oscillations.

6.3. Mixing Chamber Internal Angle Modification

The present section clarifies the fluidic oscillator performance when the mixing chamber inlet angle is modified, the main details of the different MC angles studied were already specified in Table 4. The fluidic oscillator outlet dynamic mass flow for the mixing chamber minimum and maximum angles (Angle 1) and (Angle 3), respectively, and for the standard one (STD), are presented in Figure 13a. The time dependent feedback channel mass flow measured at the lower feedback channel outlet and for the same three mixing chamber angles is introduced in Figure 13b.

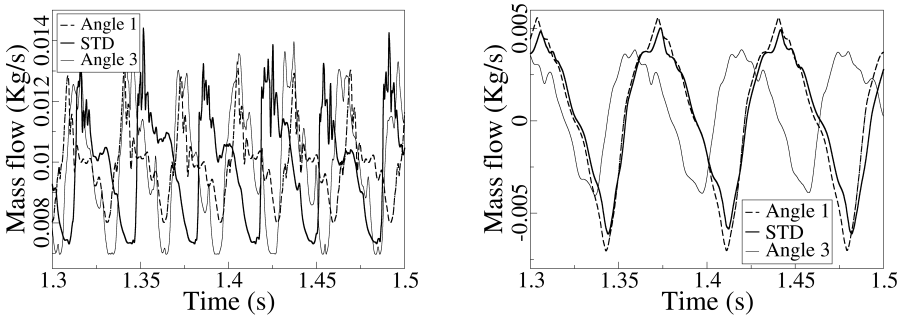

Figure 13. Fluidic oscillator outlet dynamic mass flow (a) and feedback channel mass flow (b), for the smallest mixing chamber internal angle (Angle 1), the largest MC internal angle (Angle 3) and the standard case (STD).

As the mixing chamber angle increases, the peak to peak amplitude of the FO outlet mass flow as well as its associated frequency, keep increasing. An opposite effect is observed on the FC mass flow, since the peak to peak amplitude decreases with the MC angle increase, decreasing as well the maximum reverse flow in the feedback channels, the frequency increases. The outlet mass flow peak to peak amplitude and frequency increase when comparing the minimum (Angle 1) and maximum (Angle 3) angles studied, is respectively of 46% and 15%, the corresponding FC mass flow amplitude decrease and frequency increase is of 65% and 19.5% respectively. What it is perhaps more interesting to highlight is the fact that the maximum outlet mass flow appears when the jet leaving the mixing chamber is having whether its maximum or minimum inclination angle versus the horizontal axis, this is more clearly observed when looking at the videos, (see appendix). In fact, the same was happening in Figure 4a for different Reynolds numbers and in Figure 9a, for different outlet widths. Notice that for these two figures as well as for Figure 13a, the respective minimum mass flows obey to the instants the jet leaving the FO flows horizontally, two maximum consecutive peaks characterize the instants at which the jet leaving the FO generate the maximum angles, whether positive or negative, versus the horizontal axis. This is why in all these graphs the FC mass flow seams as if the corresponding frequency was half of the FO outlet mass flow one. A final remarkable detail to be observed in Figure 13b, is that the reverse flow (flowing from the FC outlet towards the FC inlet) keeps decreasing with the increase of the MC angle. It appears as if a higher freedom in the movement associated to the jet inside the mixing chamber, reduces the reverse flow in the feedback channels, although in reality this effect will be more clearly understood when analyzing the pressure at the mixing chamber outlet inclined

Preprints (www.preprints.org) | NOT PEER-REVIEWED | Posted: 11 January 2024 doi:10.20944/preprints202401.0827.v1

walls. The dynamic maximum stagnation pressure measured at the MC outlet lower inclined wall, the pressure momentum term measured at the lower FC outlet, the mass flow momentum term measured at the same location and the net momentum acting over the jet as it enters the mixing chamber, which considers the instantaneous pressure and mass flow terms at both FC outlets, and for the same three MC angles already introduced Figure 13 are presented in Figure 14a, b, c, d, respectively. Focusing on the stagnation pressure, Figure 14a, it is observed that as the MC inclined angle increases, the stagnation pressure peak to peak amplitude decreases, the maximum pressure becomes smaller and the signal appears to be having a higher degree of randomness. A similar trend is observed when evaluating the pressure momentum term at the FC lower outlet. The trend is as well similar when considering the mass flow momentum at the FC lower outlet and the overall net momentum acting over the jet as it enters the MC, yet these two momentum signals are smoother than the previous pressure signals described, since they are obtained from the integration of the respective values across the FC outlet surfaces.

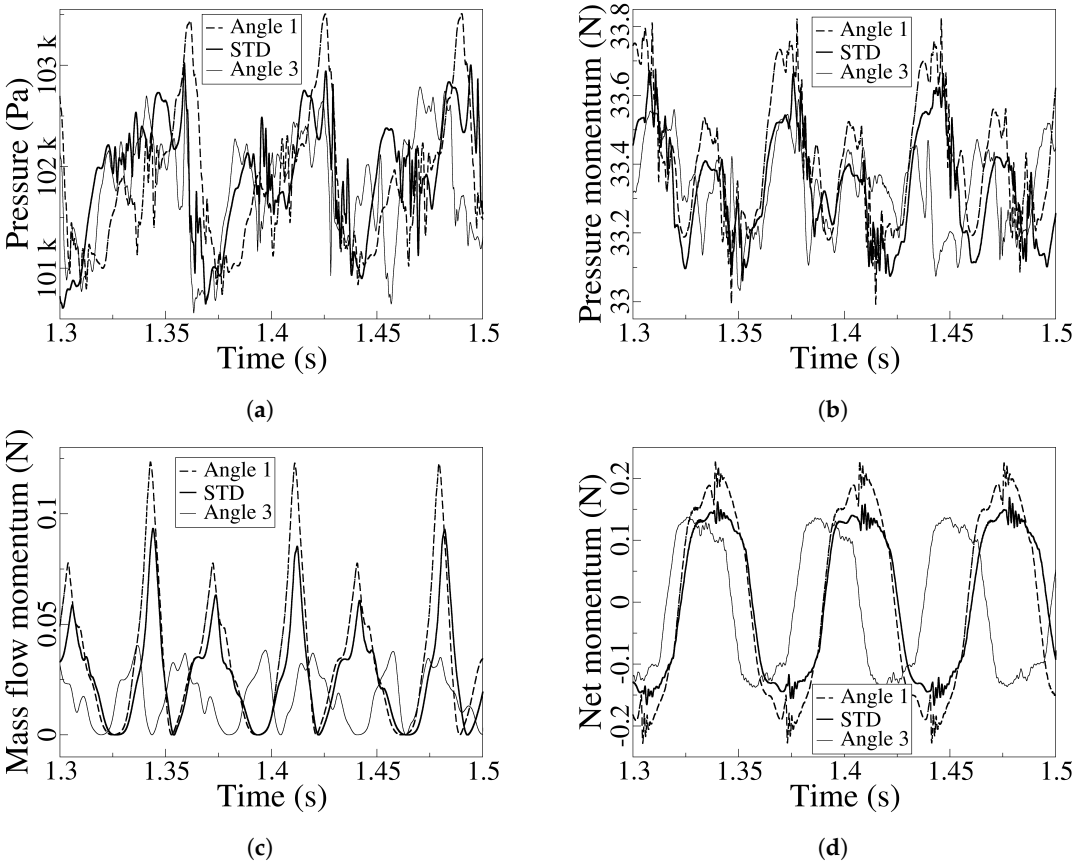

Figure 14. Stagnation pressure dynamics measured at the mixing chamber lower inclined wall (a). Pressure momentum term measured at the FC lower outlet (b). Dynamic mass flow momentum term measured at the FC lower outlet (c), and the instantaneous net momentum obtained when considering pressure and mass flow momentum terms at both FC outlets (d). All graphs consider three different MC angles, the smallest, (Angle 1), the standard case (STD) and the largest one (Angle 3) studied in the present research.

All graphs presented show an small increase of frequency as the MC inclined angle increases, when considering the FO outlet mass flow the frequency increase is about 15%, such frequency increase raises to around 20% if the FC mass flow is evaluated. As already observed when analyzing the Reynolds and the MC outlet width cases, the pressure momentum term measured at the FC lower outlet, Figure 14b, is several orders of magnitude higher than the mass flow momentum term, Figure 14c, measured at the same location. Yet, when evaluating the mass flow momentum term measured

Preprints (www.preprints.org) | NOT PEER-REVIEWED | Posted: 11 January 2024 doi:10.20944/preprints202401.0827.v1

instantaneously at both FC outlets, and comparing it with the pressure momentum term analyzed in the same location, see figures Figure 15a, b, respectively, it can be concluded that both momentum terms have the same order of magnitude. The momentum pressure term is being about 400% higher than the mass flow one.

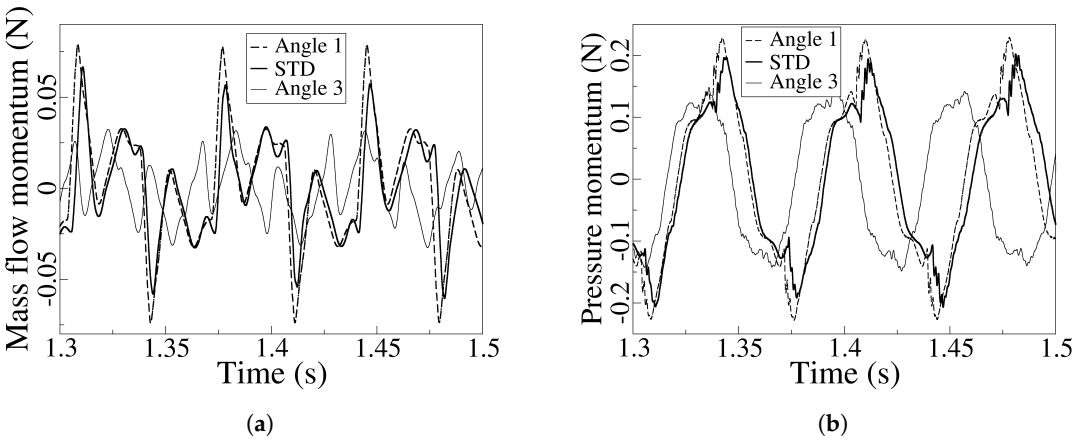

(a) (b)

Figure 15. Instantaneous momentum mass flow and pressure terms measured at both feedback channels outlet sections and for the smallest MC angle (Angle 1), the standard case (STD) and the largest MC angle (Angle 3) studied. (a) Mass flow momentum. (b) Pressure momentum.

The corresponding velocity and pressure fields for the minimum (Angle 1) and maximum (Angle 3) angles evaluated, are introduced in Figure 16. Small MC inclined angles direct the flow towards the MC outlet, this results in a higher stagnation pressure at the MC inclined wall, see Figures 16a,b and 14a. As the MC inclined angle increases, the jet inside the MC has a higher degree of freedom, this results in a higher degree on random oscillations and a smaller stagnation pressure at the MC inclined walls, see Figures 16c,d and 14a. Small MC inclined angles generate higher maximum instantaneous FO outlet velocities, but appearing just at the center of the jet, which entails smaller outlet mass flow amplitudes. Large MC inclined angles create outlet jets with much uniform velocity distributions, being the FO outlet peak to peak amplitude larger, as observed when comparing Figures 16a, c and 13a.

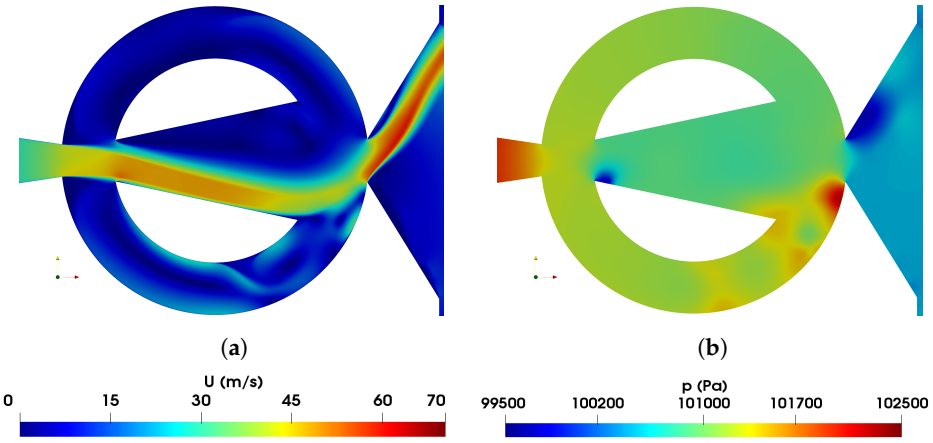

Figure 16. *Cont.*

Preprints (www.preprints.org) | NOT PEER-REVIEWED | Posted: 11 January 2024 doi:10.20944/preprints202401.0827.v1

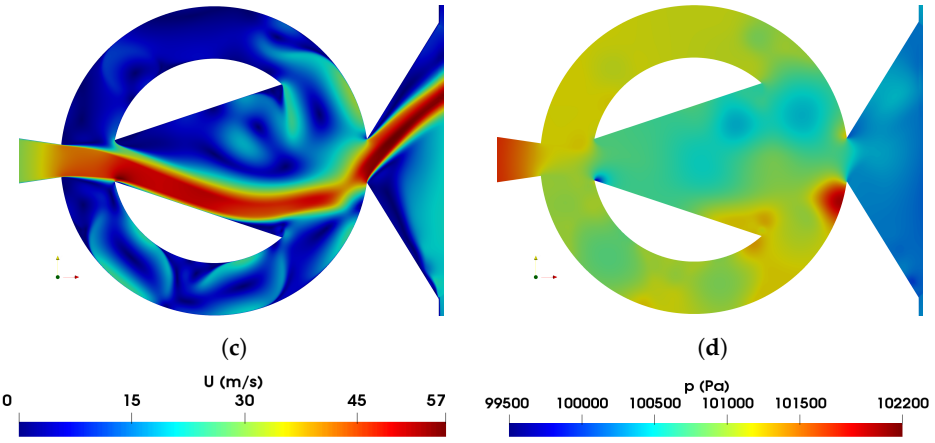

Figure 16. Fluidic oscillator internal velocity magnitude field (a, c) and pressure field (b, d). Minimum MC inclined angle (Angle 1) (a, b), Maximum MC inclined angle (Angle 3) (c, d).

7. Discussion of the Results, Origin of the Self Sustained Oscillations

Until this point, the main dynamic characteristics of the FO have been analyzed at different Reynolds numbers, outlet widths and MC inclined angles. For all cases studied, a large reverse flow at the FC has been observed, see Figure 4b, Figure 9b and Figure 13b. In fact this large reverse flow was not previously observed in the FO's configurations studied by [14,25–27], or even by [28], where the same FO configuration but at very low Reynolds number was studied. In the present subsection, half oscillation cycle is carefully analyzed, linking the velocity and pressure fields at different instants with the forces acting over the jet, the concept here is to unveil the forces acting on the jet as it enters the mixing chamber and understand why even when this large reverse flow exist, the jet keeps oscillating. Figure 17 introduces for half oscillation cycle and in separate graphs, the mass flow and pressure forces pushing the jet on each feedback channel outlet, the overall forces acting over the jet are as well presented. Five different time instants, shown as vertical lines in these graphs, will serve to analyze the dynamic forces on the jet as well as the velocity and pressure fields associated, these fields are introduced in figure Figure 18.

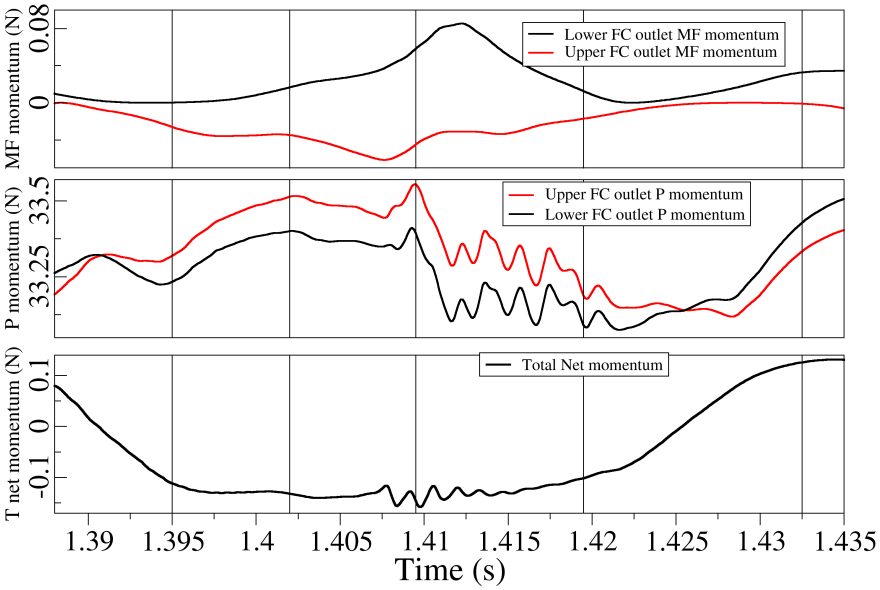

Figure 17. Dynamic mass flow and pressure momentum measured at both Feedback channel outlets and the overall momentum acting on the jet, half cycle is presented here. Baseline case configuration (STD) at Re=54595.

Preprints (www.preprints.org) | NOT PEER-REVIEWED | Posted: 11 January 2024 doi:10.20944/preprints202401.0827.v1

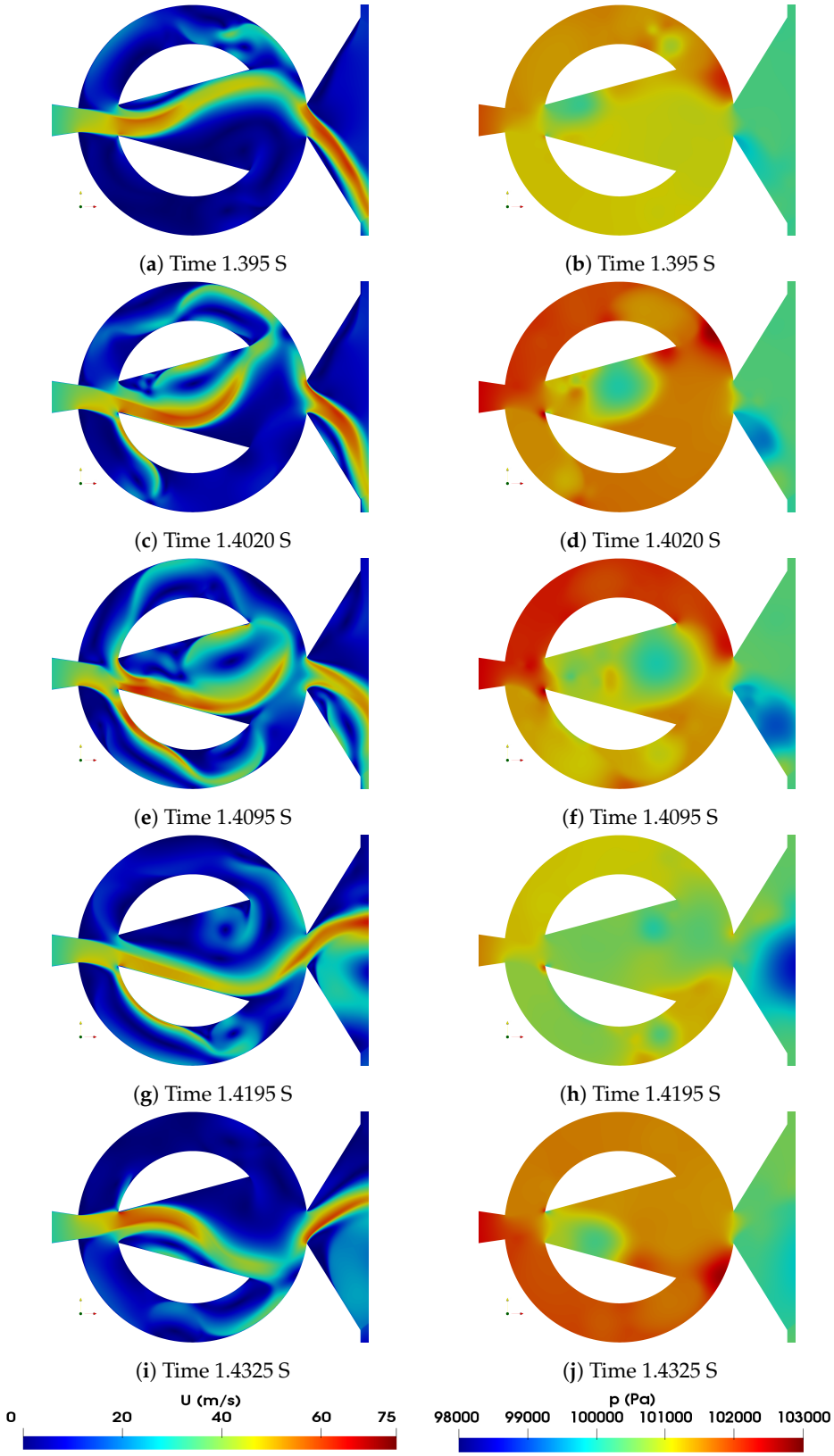

Figure 18. Velocity and pressure fields at different time steps along a half oscillation period. Baseline case (STD) at Re=54595.

Focusing initially at time 1.395*S* and looking at Figure 17, it is noticed that at this instant the mass flow forces as well as the pressure ones are pushing the jet downwards, the upper FC pressure forces

 doi:10.20944/preprints202401.0827.v1

are in reality negative, for convenience we represented both FC outlet pressure forces as positive in Figure 17. This is why the net momentum is negative, as a result the jet entering the mixing chamber is moving down, this is initially seen in Figure 18a, b, which respectively introduce the velocity and pressure fields at this instant. Notice that the upper FC is pressurized and flow moves from the upper FC inlet towards the outlet. The next time instant chosen for the evaluation is 1.402S, represented by the second vertical line in Figure 17. The pressure forces as well as the mass flow forces pushing the jet downwards are now bigger than in the previous time instant chosen, this is why the net momentum is now having a higher negative value. Looking at the velocity and pressure fields presented respectively in Figure 18c, d, it can clearly be seen that the jet has displaced downwards, a large flow moves towards the upper FC outlet, reverse flow start appearing at the lower feedback channel and the pressure along the entire upper FC is higher than the one observed in the previous instant examined. It is also relevant to highlight that the small vortical structure initially appearing at the entrance upper side of the mixing chamber has now moved downstream inside the mixing chamber and it is bending the jet inside the mixing chamber upwards. Moving now to time 1.4095 seconds, the third vertical line in Figure 17, it is observed that at this instant the mass flow forces pushing the jet downwards are almost maximum, the pressure at the upper FC outlet has reached its maximum value, but the pressure drop between the upper and lower FC outlet is similar than in the previous time analyzed, notice the upper FC is highly pressurized Figure 18f. The reverse flow at the lower FC is now as well maximum, Figure 18e, and this reverse flow is now interacting with the main jet inside the mixing chamber, generating the pressure oscillations observed in figure Figure 17. Such pressure disturbance generated mainly by the reverse flow in the lower FC is the precursor of the jet flipping inside the MC. As a matter of a fact, in the next time evaluated, 1.4195 seconds, the jet inside the MC starts moving upwards, the reverse mass flow in the lower FC has decreased, an stagnation pressure area is appearing at the MC outlet lower inclined wall, see Figure 18g, h, yet as observed in figure Figure 17 the pressure and mass flow forces appear to be slightly pushing the jet downwards. In Figure 18g, h, can still be seen how the pressure at the upper FC outlet is slightly higher than the one at the lower FC one. We can therefore hypothesize that the change of flipping direction of the jet inside the MC starts downstream of the mixing chamber, due to the stagnation area generated at the MC inclined wall. Finally, at time 1.4329 seconds, the entire lower FC is pressurized, the pressure and mass flow forces are pushing he jet upwards and a small vortical structure is beginning to generate below the jet inside the MC. This time represents a similar status than the one observed in Figure 18a, b, but when the jet was moving downwards.

8. Conclusions

This paper presents a rather new configuration of a Fluidic Oscillator characterized by it simplicity and having wide and short Feedback Channels. Analysis has been performed for different incoming flow Reynolds numbers, different outlet widths and several Mixing Chamber inclined angles. Despite its simplicity the FO presents a very good linearity between the output flow frequency and the incoming Reynolds number. Regardless of the case studied, the onset of the self sustained oscillations is proven to be mostly due to the pressure forces acting onto the jet as it enters the mixing chamber, the forces due to the mass flow, although smaller, have for the present configuration the same order of magnitude as the pressure ones. This is at odds to what was previously observed in [25–27], where the self-sustained oscillations were pressure driven and the mass flow forces had a minor influence, but the FO studied in these references was a completely different one having much longer and narrower feedback channels than the ones studied here. Another characteristic which differentiates the present configuration from the previous studied ones is the large reverse flow existing in the feedback channels, we have proven that this reverse flow interacts with the main jet inside the mixing chamber generating random pressure fluctuations in the mixing chamber, this happens just before the jet flips towards the opposite direction. The Reynolds number increase, generates an increase of the outlet mass flow and feedback channel mass flow amplitude, the pressure inside the mixing chamber is also rising. The forces acting on the jet also raise with the Reynolds number. The outlet width increase, has associated

an increase of the outlet mass flow amplitude, yet the feedback channel mass flow suffers minor modifications. The stagnation pressure inside the MC as well as its peak to peak amplitude keep decreasing with the outlet width increase. The same trend is observed from the pressure forces acting on a FC outlet. When considering the modification of the mixing chamber internal angle, it is observed that larger MC internal angles have associated larger outlet mass flow peak to peak amplitudes and smaller amplitudes of the feedback channel mass flow, reducing as well the reverse flow in the FC. Pressure forces and mass flow forces acting on the jet as it enters the MC are also reduced with the MC internal angle increase.

Supplementary Materials: The following supporting information can be downloaded at the website of this paper posted on Preprints.org. A set of four videos introducing the flow and pressure fields initially presented in Figure 8 at Reynolds numbers 27483 and 68707 are here introduced. A second set of six velocity and pressure field videos presented here, correspond to the standard, maximum and minimum outlet widths and for a constant Reynolds number of 54595, Figure 12 introduced instant fields for these three cases. The final four videos given as supplementary material, characterize the flow and pressure fields inside the FO for the minimum and maximum MC inclined angles studied. Figure 16 introduced these velocity fields. It is important to notice that for all the cases studied, a large reverse flow is observed inside the FC's.

Author Contributions: Conceptualization, JM.B.; methodology, K.K. and JM.B.; software, K.K.; validation, K.K. and JM.B.; formal analysis, K.K. and JM.B.; investigation, K.K. and JM.B.; data curation, K.K.; writing—original draft preparation, JM.B.; M.M. and K.K.; writing—review and editing, JM.B.; visualization, K.K. and JM.B.; supervision, JM.B. and M.M; project administration, JM.B.; funding acquisition, JM.B.

Funding: No funding was received for this project.

Institutional Review Board Statement: Not applicable.

Informed Consent Statement: Not applicable.

Data Availability Statement: Not applicable.

Conflicts of Interest: The authors declare no conflicts of interest.

References

1. Ostermann, F.; Woszidlo, R.; Nayeri, C.N.; Paschereit, C.O. Properties of a sweeping jet emitted from a fluidic oscillator. *Journal of Fluid Mechanics* **2018**, *857*, 216–238.
2. Zeleke, D.S.; Huang, R.F.; Hsu, C.M. Effects of Reynolds number on flow and mixing characteristics of a self-sustained swinging jet. *Journal of Turbulence* **2020**, *21*, 434–462.
3. Kim, M.; Kim, D.; Yeom, E.; Kim, K.C. Experimental study on heat transfer and flow structures of feedback-free sweeping jet impinging on a flat surface. *International Journal of Heat and Mass Transfer* **2020**, *159*, 120085.
4. Mohammadshahi, S.; Samsam-Khayani, H.; Cai, T.; Nili-Ahmadabadi, M.; Kim, K.C. Experimental study on flow characteristics and heat transfer of an oscillating jet in a cross flow. *International Journal of Heat and Mass Transfer* **2021**, *173*, 121208.
5. Handa, T.; Fujimura, I. Fluidic oscillator actuated by a cavity at high frequencies. *Sensors and Actuators A: Physical* **2019**, *300*, 111676.
6. Suh, J.; Han, K.; Peterson, C.W.; Bahl, G. Invited Article: Real-time sensing of flowing nanoparticles with electro-opto-mechanics. *APL photonics* **2017**, *2*.
7. Guha, S.; Schmalz, K.; Wenger, C.; Herzel, F. Self-calibrating highly sensitive dynamic capacitance sensor: Towards rapid sensing and counting of particles in laminar flow systems. *Analyst* **2015**, *140*, 3262–3272.
8. Kim, S.; Kihm, K.D.; Thundat, T. Fluidic applications for atomic force microscopy (AFM) with microcantilever sensors. *Experiments in fluids* **2010**, *48*, 721–736.
9. Länge, K.; Blaess, G.; Voigt, A.; Götzen, R.; Rapp, M. Integration of a surface acoustic wave biosensor in a microfluidic polymer chip. *Biosensors and Bioelectronics* **2006**, *22*, 227–232.
10. Sakong, J.; Roh, H.; Roh, Y. Surface acoustic wave DNA sensor with micro-fluidic channels. *Japanese Journal of Applied Physics* **2007**, *46*, 4729.
11. Kim, S.H.; Kim, K.Y. Effects of installation location of fluidic oscillators on aerodynamic performance of an airfoil. *Aerospace Science and Technology* **2020**, *99*, 105735.

12. Cerretelli, C.; Wuerz, W.; Gharaibah, E. Unsteady separation control on wind turbine blades using fluidic oscillators. *AIAA journal* **2010**, *48*, 1302–1311.
13. Tousi, N.; Coma, M.; Bergadà, J.; Pons-Prats, J.; Mellibovsky, F.; Bugeda, G. Active flow control optimisation on SD7003 airfoil at pre and post-stall angles of attack using synthetic jets. *Applied Mathematical Modelling* **2021**, *98*, 435–464.
14. Bobusch, B.C.; Woszidlo, R.; Bergada, J.M.; Nayeri, C.N.; Paschereit, C.O. Experimental study of the internal flow structures inside a fluidic oscillator. *Experiments in fluids* **2013**, *54*, 1559.
15. Vatsa, V.; Koklu, M.; Wygnanski, I. Numerical simulation of fluidic actuators for flow control applications. 6th AIAA Flow Control Conference, 2012, p. 3239.
16. Ostermann, F.; Woszidlo, R.; Nayeri, C.; Paschereit, C.O. Experimental comparison between the flow field of two common fluidic oscillator designs. 53rd AIAA Aerospace Sciences Meeting, 2015, p. 0781.
17. Aram, S.; Lee, Y.T.; Shan, H.; Vargas, A. Computational Fluid Dynamic Analysis of Fluidic Actuator for Active Flow Control Applications. *AIAA Journal* **2017**, pp. 1–10.
18. Woszidlo, R.; Ostermann, F.; Nayeri, C.; Paschereit, C. The time-resolved natural flow field of a fluidic oscillator. *Experiments in Fluids* **2015**, *56*, 125.
19. Gaertlein, S.; Woszidlo, R.; Ostermann, F.; Nayeri, C.; Paschereit, C.O. The time-resolved internal and external flow field properties of a fluidic oscillator. 52nd Aerospace Sciences Meeting, 2014, p. 1143.
20. Slupski, B.Z.; Kara, K. Effects of Geometric Parameters on Performance of Sweeping Jet Actuator. 34th AIAA Applied Aerodynamics Conference, 2016, p. 3263.
21. Wang, S.; Baldas, L.; Colin, S.; Orieux, S.; Kourta, A.; Mazellier, N. Experimental and numerical study of the frequency response of a fluidic oscillator for active flow control. 8th AIAA Flow Control Conference, 2016, p. 4234.
22. Pandey, R.J.; Kim, K.Y. Numerical modeling of internal flow in a fluidic oscillator. *Journal of Mechanical Science and Technology* **2018**, *32*, 1041–1048.
23. Seo, J.; Zhu, C.; Mittal, R. Flow Physics and Frequency Scaling of Sweeping Jet Fluidic Oscillators. *AIAA Journal* **2018**, pp. 1–12.
24. Bobusch, B.C.; Woszidlo, R.; Krüger, O.; Paschereit, C.O. Numerical Investigations on Geometric Parameters Affecting the Oscillation Properties of a Fluidic Oscillator. 21st AIAA Computational Fluid Dynamics Conference, 2013, p. 2709.
25. Baghaei, M.; Bergada, J.M. Analysis of the Forces Driving the Oscillations in 3D Fluidic Oscillators. *Energies* **2019**, *12*, 4720.
26. Baghaei, M.; Bergada, J.M. Fluidic Oscillators, the Effect of Some Design Modifications. *Applied Sciences* **2020**, *10*, 2105.
27. Bergadà, J.M.; Baghaei, M.; Prakash, B.; Mellibovsky, F. Fluidic oscillators, feedback channel effect under compressible flow conditions. *Sensors* **2021**, *21*, 5768.
28. Sarwar, W.; Bergadà, J.M.; Mellibovsky, F. Onset of temporal dynamics within a low reynolds-number laminar fluidic oscillator. *Applied Mathematical Modelling* **2021**, *95*, 219–235.
29. Lee, S.; Roh, T.S.; Lee, H.J. Influence of jet parameters of fluidic oscillator-type fuel injector on the mixing performance in a supersonic flow field. *Aerospace Science and Technology* **2023**, *134*, 108154.
30. Tavakoli, M.; Nili-Ahmadabadi, M.; Joulaei, A.; Ha, M.Y. Enhancing subsonic ejector performance by incorporating a fluidic oscillator as the primary nozzle: a numerical investigation. *International Journal of Thermofluids* **2023**, *20*, 100429.
31. Menter, F. Zonal two equation kw turbulence models for aerodynamic flows. 23rd fluid dynamics, plasmadynamics, and lasers conference, 1993, p. 2906.